Electric-field-driven Deterministic and Robust 120° Magnetic Rotation in a Concave Triangular Nanomagnet

Ren-Ci Peng,[1] Long-Qing Chen,[2] Ziyao Zhou,[1] Ming Liu,[1,*] and Ce-Wen Nan[3,†]

[1]*Electronic Materials Research Laboratory, Key Laboratory of the Ministry of Education & International Center for Dielectric Research, School of Electronic Science and Engineering, Faculty of Electronic and Information Engineering, Xi'an Jiaotong University, Xi'an 710049, China*

[2]*Department of Materials Science and Engineering, The Pennsylvania State University, University Park, Pennsylvania 16802, USA*

[3]*State Key Lab of New Ceramics and Fine Processing, School of Materials Science and Engineering, Tsinghua University, Beijing 100084, PR China*

Deterministic magnetic switching driven by electric fields rather than power-dissipating currents at the nanoscale is fundamentally challenging yet promising for applications to energy-efficient and high-density spintronic devices. Here, we demonstrate an electric-field-controlled deterministic, robust and repeatable 120° rotation of "Y"-like magnetic state in a patterned nanoscale multiferroic heterostructure consisting of a concave triangular nanomagnet deposited on $Pb(Mg_{1/3}Nb_{2/3})O_3$-$PbTiO_3$ film. Using phase-field simulations, we find that the rotation of "Y"-like magnetic state is controlled by a co-action of strain-mediated electric-field-induced uniaxial magnetoelastic anisotropy, magnetic in-plane shape anisotropy of the concave-triangle-shaped nanomagnet, and an interfacial exchange-bias field from a juxtaposed antiferromagnetic layer. It is also shown that deterministic magnetic state switching can be accomplished by a pulsed strain, the duration of which can span from ten nanoseconds or longer down to a few nanoseconds, providing great design flexibility. We also discuss the dynamics of electric-field-driven switching of "Y"-like magnetic state as well as the influence of side length, thickness, and shape variation (i.e., concave radius) of the nanomagnet on the critical strain for the switching. These results offer a technologically viable route to designing nanomagnet-based nonvolatile spin memories with high density and low power.

I. INTRODUCTION

Multiferroic heterostructures, integrating ferromagnetic and ferroelectric materials via interfacial coupling, have sparked substantial interest because of not only abundant physical phenomena emerging from the interface between ferromagnetic and ferroelectric orders but also the intriguing technological potential in low-energy-consumption spintronics, such as spin memories [1–5], logic devices [5,6], and sensors [7,8]. The manipulation of magnetism with an electric field rather than a heat-dissipating electric current can be enabled by the magnetoelectric coupling effect in insulating multiferroic heterostructures, which will be a promising energy-efficient avenue to encoding data in a next-generation high-density magnetoelectric random access memory. In the last decade, research into electric-field-manipulated magnetic switching (including the rotation of magnetization) has gained great momentum in multiferroic heterostructures, and several mechanisms have been proposed, such as the transfer of the interfacial strain [9–14], interfacial exchange coupling or bias [15,16], and interfacial charge and orbital mediation [17,18]. For example, Ghidini *et al.* directly observed strain-mediated electric-field-driven switching of local magnetization in multilayer capacitors comprised of Ni electrode layers and a $BaTiO_3$ layer in the presence of a static in-plane magnetic field [9]. Recently, a more pioneering experimental achievement demonstrated purely electrically driven switching of in-plane net magnetization in an exchange-coupled heterostructure consisting of a micron-sized $Co_{0.9}Fe_{0.1}$ magnet and a $BiFeO_3$ film [15].

In spite of the aforementioned intriguing experiments in the continuous film-based multiferroic heterostructures, there are quite a few studies of electric-field-driven magnetic switching in the patterned nanoscale multiferroic heterostructures [2,13], which is technologically important for both low-power and ultrahigh-density integration memory applications. Moreover, the investigation of electric-field-driven magnetic switching in nanoscale heterostructures is fundamentally fascinating, because scaling down the

* mingliu@xjtu.edu.cn
† cwnan@tsinghua.edu.cn

dimension of a magnet to nanometers produces diversities of exotic magnetic states arising from distinct size effects and strong magnetic shape anisotropy of the nanoscale magnet. For example, in the triangle-shaped nanomagnets [19–24], bucklelike [19], "Y"-like [19,24], and even vortex [21–23] magnetic ground states depending on their geometry and size were observed. Therefore, fundamentally understanding the mechanism of electric-field-driven magnetic switching in patterned nanoscale multiferroic heterostructures is highly pressing for realizing high-density and ultralow-power memories.

Very recently, electric-field-driven 120° rotation of magnetic state has been observed experimentally in a nanoscale multiferroic heterostructure comprised of triangular Co nanodots and a tetragonal BiFeO₃ film [25], but this rotation was not deterministic because only the specific type of ferroelectric polarization switching resulted in the reorientation of the canted magnetic moment in BiFeO₃ film [26] and not every Co nanodot with the same initial magnetic state accomplished the same rotation driven by an electric field pulse. Theoretically, strain-mediated electrically driven magnetic switching has been demonstrated by magnetization precession via precisely controlling the duration of strain pulse in nanomagnets [27–29], but the narrow window of strain pulse is challenging for enabling low-error-rate practical applications. Overall, an experimental or theoretical demonstration of electrically driven deterministic and robust magnetic switching in nanoscale multiferroic heterostructures that is favorable in high-density data storage remains lacking.

In this work, we computationally accomplish an electrically driven deterministic, robust, and repeatable 120° rotation of "Y"-like magnetic state via the heterostructure design. Figure 1(a) illustrates the proposed patterned nanoscale multiferroic heterostructure that is comprised of an equilateral triangular amorphous nanomagnet with concave arcs sandwiched by an overlying antiferromagnetic layer and an underlying (011)-Pb(Mg$_{1/3}$Nb$_{2/3}$)O$_3$-PbTiO$_3$ (PMN-PT) film. Here, (011)-PMN-PT film is chosen as the ferroelectric layer because PMN-PT nearby the morphotropic phase boundary possesses a large piezoelectric effect [30] and Terfenol-D is employed as a model magnetic material due to its giant magnetostrictive coefficient at room temperature [31], allowing for robust strain-mediated magnetoelectric coupling. It was previously reported that "Y"-like magnetic state can be stabilized by introducing concavity in the triangle-shaped nanomagnet [24]. Hence, here the triangle-shaped nanomagnet with concave arcs is selected to study the effect of shape anisotropy on "Y"-like magnetic state and its dynamical switching via varying the concave radius, side length, and thickness of the nanomagnet. Using phase-field simulations, we find that the rotation of "Y"-like magnetic state [see Fig. 1(c)] can be controlled by a congenerous effect of electrically induced
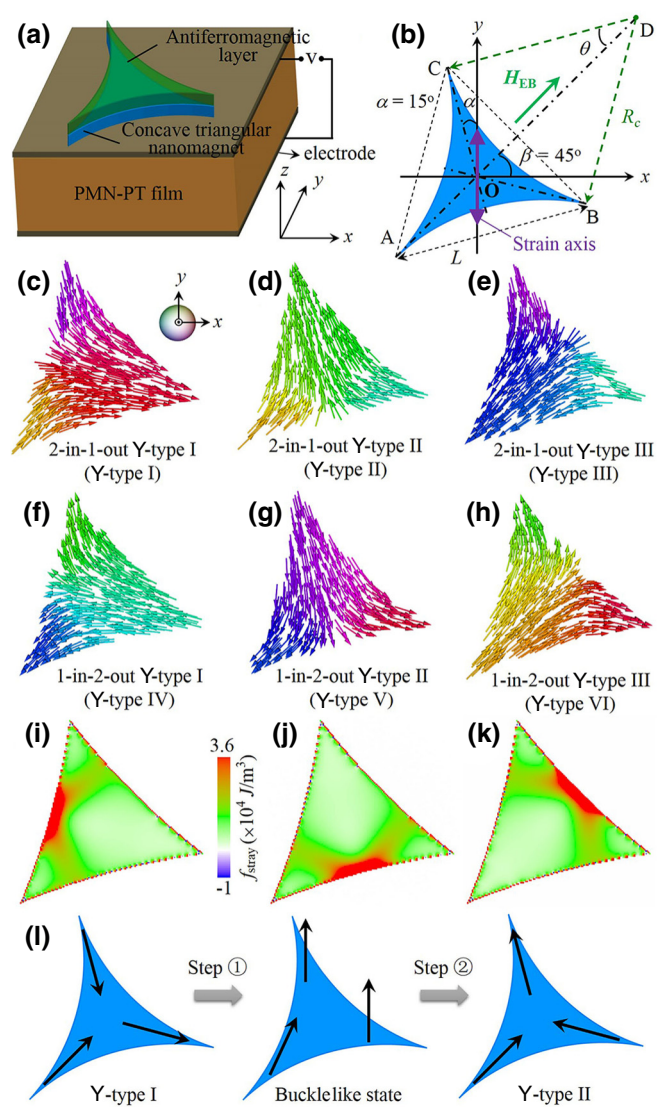

FIG. 1. (a) Schematic of nanoscale magnetoelectric heterostructure consisting of a concave triangular amorphous Terfenol-D nanomagnet on top of PMN-PT ferroelectric film. (b) Vertical view of the concave-triangle-shaped nanomagnet canted by $\alpha = 15°$ to the $+y$ axis with a concave radius R_c, where H_{EB} is an exchange-bias field at an angle $\beta = 45°$ to the $+x$ axis in the x-y plane. (c)–(h) Six degenerate states of the initial "Y"-like magnetic states with $H_{EB} = 0$ and $R_c = 600$ nm, where (c)–(e) denote three 2-in-1-out Y-type magnetic states (namely, Y-type I, Y-type II, and Y-type III) and (f)–(h) represent another three 1-in-2-out Y-type magnetic states (namely, Y-type IV, Y-type V, and Y-type VI). (i)–(k) Spatial distributions of stray-field energy density corresponding to three equivalent states of (c)–(e), respectively. (l) A two-step principle of "Y"-like magnetic state switching from Y-type-I state to Y-type-II state.

strain-mediated uniaxial magnetoelastic anisotropy, magnetic in-plane shape anisotropy of the concave-triangle-shaped nanomagnet, and an interfacial exchange-bias field from the interface between the antiferromagnet and the nanomagnet.

II. METHODS

The switching of "Y"-like magnetic state with an electric field is performed by phase-field simulations. In our phase-field model, we employ the local magnetization vector $\mathbf{M} = M_s(m_x, m_y, m_z)$ as the primary order parameter, where M_s denotes the saturation magnetization of the amorphous Terfenol-D. Magnetic domains are represented by spatial distributions of $\mathbf{M}$. The temporal and spatial evolution of the local magnetization vector $\mathbf{M}$ in the Terfenol-D nanomagnet can be acquired by numerically solving the Landau-Lifshitz-Gilbert equation [32],

$$(1 + \alpha^2)\frac{\partial \mathbf{M}}{\partial t} = -\gamma_0(\mathbf{M} \times \mathbf{H}_{\text{eff}}) - \frac{\gamma_0 \alpha}{M_s}\mathbf{M} \times (\mathbf{M} \times \mathbf{H}_{\text{eff}}), \tag{1}$$

where α and γ_0 signify the Gilbert damping coefficient and the gyromagnetic ratio, respectively. The effective magnetic field is determined by $\mathbf{H}_{\text{eff}} = -(1/\mu_0)(\delta F_{\text{tot}}/\delta \mathbf{M})$, where μ_0 represents the vacuum permeability, and F_{tot} is the total free energy of the Terfenol-D nanomagnet. The real-time step (Δt) correlated with the dimensionless numerical time step ($\Delta \tau = 0.02$) is about 0.103 ps through $\Delta t = \Delta \tau (1 + \alpha^2)/(\gamma_0 M_s)$. For the concave triangular Terfenol-D amorphous nanomagnet deposited on a PMN-PT film, F_{tot} can be expressed as

$$F_{\text{tot}} = \iiint_V (f_{\text{stray}} + f_{\text{elast}} + f_{\text{exch}} + f_{\text{EB}})dV, \tag{2}$$

where f_{stray}, f_{elast}, f_{exch}, and f_{EB} represent the local densities of stray field, elastic, exchange, exchange-bias-related energy, respectively. f_{EB} can be given by

$$f_{\text{EB}} = -H_{\text{EB}}M_s\left[\frac{\sqrt{2}}{2}(m_x + m_y) - 1\right], \tag{3}$$

where H_{EB} denotes an interfacial exchange-bias field between the triangle nanomagnet and the upper antiferromagnet at an angle $\beta = 45°$ away from the $+x$ axis in the x-y plane [see Fig 1(b)]. f_{stray} is related to the shape of the nanomagnet and is solved with a finite-size-magnet magnetostatic boundary condition [33]. The mathematical expression of f_{stray} in the nanomagnet can be found in Ref. [32]. f_{exch} can be expressed as

$$f_{\text{exch}} = A_{\text{ex}}|\nabla \mathbf{m}|^2, \tag{4}$$

where A_{ex} denotes the exchange constant. The elastic energy density f_{elast} is written as

$$f_{\text{elast}} = \frac{1}{2}c_{ijkl}(\varepsilon_{ij} - \varepsilon_{ij}^0)(\varepsilon_{kl} - \varepsilon_{kl}^0),$$

$$\varepsilon_{ij}^0 = \frac{3}{2}\lambda_s\left(m_i^2 - \frac{1}{3}\right), \quad i = j, \tag{5}$$

$$\varepsilon_{ij}^0 = \frac{3}{2}\lambda_s m_i m_j, \quad i \neq j,$$

$$\varepsilon_{ij} = \varepsilon_{ij}^{\text{hom}} + \varepsilon_{ij}^{\text{het}},$$

where $\mathbf{c}$ represents the four-rank elastic stiffness tensor of the amorphous Terfenol-D, ε_{ij}^0 indicates the eigenstrain or stress-free strain due to magnetostriction, λ_s is the saturation magnetostriction; the total strain $\boldsymbol{\varepsilon}$ consists of a homogeneous strain $\boldsymbol{\varepsilon}^{\text{hom}}$ and a heterogeneous strain $\boldsymbol{\varepsilon}^{\text{het}}$ according to Khachaturyan's theory of microelasticity [34]. For an isotropic Terfenol-D magnet with a cubic crystal, the elastic stiffness coefficients (c_{ijkl}) for the actual tensor $\mathbf{c}$ can be simplified as c_{ij} with its three independent coefficients c_{11}, c_{12}, and c_{44} in Voigt's notation (see Supplemental Material [35] for details). $\boldsymbol{\varepsilon}^{\text{hom}}$ denotes the macroscopic deformation, arising from the applied strain [i.e., the anisotropic piezostrain ($\varepsilon_{yy} - \varepsilon_{xx}$) assumed from the ferroelectric PMN-PT film]. $\boldsymbol{\varepsilon}^{\text{het}}$ describes the local deformation with a zero volumetric integral (namely, $\int \varepsilon_{ij}^{\text{het}}(r)dV = 0$), and can be determined by solving the mechanical equilibrium equation $\nabla \cdot [c_{ijkl}\varepsilon_{kl}^{\text{het}} - c_{ijkl}(\varepsilon_{kl}^0 - \varepsilon_{kl}^{\text{hom}})] = 0$. PMN-PT film that can generate giant electric-field-induced strain via non-180° polarization switching [30] is considered as a candidate of the ferroelectric layer. This work is centered on the computation demonstration of the critical strain required for Y-type magnetic state switching, and the process of generating strain under the application of an electric field to PMN-PT film is not investigated for simplicity.

Three-dimensional discrete grids of $154\Delta x \times 154\Delta y \times 60\Delta z$ with a real grid space $\Delta z = 0.5$ nm and $\Delta x = \Delta y = 1.0$ nm as an example are utilized for the simulations. The bottom grids of $154\Delta x \times 154\Delta y \times 45\Delta z$ are used to describe the PMN-PT ferroelectric film, the top grids of $154\Delta x \times 154\Delta y \times 5\Delta z$ are designated as the air layer, and the remaining grids of $154\Delta x \times 154\Delta y \times 10\Delta z$ are employed to describe the concave triangular Terfenol-D nanomagnet with a thickness of d ($= 10\Delta z = 5$ nm) and the air layer surrounding the Terfenol-D in the middle for simulations. When size effects of the nanomagnet on magnetic state switching are investigated, different three-dimensional discrete grids will be utilized by varying the number of grids or the grid sizes (Δx, Δy, and Δz). For the sake of simplicity, the antiferromagnetic layer is not taken into account by the grids. The air grid and the bottom grid (i.e., ferroelectric layer) permit us to accommodate the three-dimensional magnetic stray field surrounding the Terfenol-D nanomagnet in simulations. The air grid permits generating stress-free top and lateral surfaces in the nanomagnet, giving rise to nonuniform strain distribution in the nanomagnet [12]. The mechanical boundary conditions on the nanomagnet-ferroelectric interface are specified with the average in-plane strain from the anisotropic piezostrain of the ferroelectric film. Periodic

mechanical boundary conditions are applied at the vertical boundaries of the ferroelectric layer in the phase-field model. Due to the bottom surface of the nanomagnet constrained by the ferroelectric layer, the ferroelectric layer is involved in solving elastic perturbation that results from the heterogeneous strain $\boldsymbol{\varepsilon}^{\mathbf{het}}$ in the nanomagnet. For the island-on-substrate system, the thickness of the substrate grid should be larger than the corresponding critical value (approximately 25 grids for our system; see Supplemental Material [35] for details) because the elastic perturbation arising from the heterogeneous strain $\boldsymbol{\varepsilon}^{\mathbf{het}}$ vanishes in the ferroelectric beyond this distance [36] and strain relaxation in the nanomagnet shows little changes as shown in the Supplemental Material [35]. In our system, the thickness of the ferroelectric grid is taken as 45 grids, much larger than the critical value of 25 grids; hence, the influence of thickness of the ferroelectric layer on the strain of the nanomagnet can be neglected.

Note that the real grid sizes (Δx, Δy, and Δz) are smaller than the exchange length of Terfenol-D ($l_{\text{ex}} \approx 4.73$ nm calculated by the formula of $l_{\text{ex}} = \sqrt{A/(0.5\mu_0 M_s^2)}$ [37]). Hence the local magnetization vectors are largely parallel to each other across the entire thickness (see Supplemental Material [35] for details). The shape of the concave triangular nanomagnet is delineated by three shape functions:

$$\left(x - 5 - \frac{L}{2}\cos 15° - R_c \cos\theta \sin 15°\right)^2$$
$$+ \left(y - 5 - \frac{L}{2}\sin 15° + R_c \cos\theta \cos 15°\right)^2 >= R_c^2, \quad (6)$$

$$\left(x - 5 - \frac{L}{2}\sin 15° + R_c \cos\theta \cos 15°\right)^2$$
$$+ \left(y - 5 - \frac{L}{2}\cos 15° - R_c \cos\theta \sin 15°\right)^2 >= R_c^2, \quad (7)$$

$$\left(x - 5 - \frac{\sqrt{6}}{4}L - R_c \cos\theta \sin 45°\right)^2$$
$$+ \left(y - 5 - \frac{\sqrt{6}}{4}L - R_c \cos\theta \sin 45°\right)^2 >= R_c^2, \quad (8)$$

where θ is a half of the central angle [$\theta = \arcsin(L/2R_c)$], L denotes the side length of the equilateral triangle, and R_c represents the radius of the concave circle, as shown in Fig. 1(b). The material parameters of Terfenol-D utilized for the simulations are collected from the literature, and the saturated magnetization, saturation magnetostriction, elastic stiffness coefficients, gyromagnetic ratio, Gilbert damping coefficient, and exchange coefficient of Terfenol-D nanomagnet are as follows: $M_s = 8 \times 10^5$ A/m [32];

$\lambda_s = 320 \times 10^{-6}$ [31]; $c_{11} = 141.0$ GPa, $c_{12} = 64.8$ GPa, and $c_{44} = 38.1$ GPa [32]; $\gamma_0 = 2.43 \times 10^5$ m/(A s) [38]; $\alpha = 0.06$ [39]; $A_{\text{ex}} = 9 \times 10^{-12}$ J/m [39].

III. RESULTS AND DISCUSSION

In Fig. 1(b), the geometric symmetry axis of the concave triangle is aligned at an angle $\beta = 45°$ away from the $+x$ axis, which makes sure that the critical strains required for the switching between two types of 2-in-1-out "Y"-like magnetic states (e.g., Y-type-I-to-Y-type-II and reversely Y-type-II-to-Y-type-I) keep the same magnitude and that three concave arcs of the triangle are comparable smooth for the grid discretization. The "Y"-like magnetic states possess six degenerate states under the exchange-bias field of $H_{\text{EB}} = 0$, as shown in Figs. 1(c)–1(h).

Among six of them, the Y-type-I magnetic state in Fig. 1(c) is selected as the exemplary initial state for the simulations, acquired by the application of a magnetic field at the $+x$ axis to generate a uniformly magnetized state and the subsequent removal of the magnetic field. The in-plane shape anisotropy is shown by the distribution of stray-field energy density of the initial state in Figs. 1(i)–1(k). It also reveals that the intrinsic easy axis in concave triangular nanomagnets lies along the bisector of the triangle because of local stray-field energy possessing the lowest value, in agreement with previous experiments [20]. As schematically seen from Fig. 1(l), switching the "Y"-like magnetic state by electrically induced piezostrain is associated with two dynamic procedures: (i) the application of an in-plane uniaxial piezostrain at the y axis to convert the Y-type-I magnetic state into a bucklelike magnetic state, which is achieved via the synergistic effect of the H_{EB} and strain-mediated uniaxial magnetoelastic anisotropy at the y axis; (ii) the removal of the uniaxial piezostrain results in the creation of the Y-type-II magnetic state driven by minimizing shape-anisotropy-related stray-field energy.

Typically, the strain transferred from the ferroelectric film is partially relaxed in the nanomagnet because of the stress-free top surface and lateral surfaces of the nanomagnet (see Supplemental Material [35] for details) [40]. Nevertheless, the high ratio of unrelaxed strain and thermodynamically stable initial magnetic state are desirable for effectively achieving a strain-mediated "Y"-like magnetic state switching. Here, two diagrams of ratio of unrelaxed strain and the initial magnetic state as a function of the side length L and the thickness d of the nanomagnet are constructed, as shown in Figs. 2(a) and 2(b), respectively. A higher ratio of unrelaxed strain appears in the nanomagnet with larger L and smaller d [see Fig. 2(a)]. There exist two stable magnetic ground states, namely, Y-type-I state and Y-type-VI state, seen from phase diagram of the initial magnetic states with $H_{\text{EB}} = 120$ Oe in Fig. 2(b). When the H_{EB} is applied for the initial Y-type-I magnetic state, it makes the Y-type-I state further evolve into an
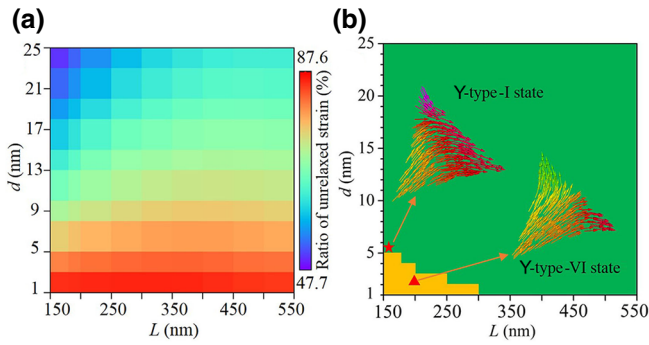
FIG. 2. (a) Ratio of unrelaxed strain ($=\varepsilon_{\mathrm{ave}}/\varepsilon_{\mathrm{appl}}$) as a function of the side length (L) and thickness (d) of the concave triangular nanomagnet at $R_c = 600$ nm. $\varepsilon_{\mathrm{ave}}$ denotes the average of the actual strain (subtracting the relaxed strain from the applied strain $\varepsilon_{\mathrm{appl}}$) in the nanomagnet. (b) Phase diagram of the initial magnetic states varying with L and d when H_{EB} is 120 Oe and R_c is 600 nm. The stable ground state is either Y-type-I or Y-type-VI state marked by a red pentagram or a red triangle, respectively.

energetically stable magnetic state. For the nanomagnets with larger d and L under $H_{\mathrm{EB}} = 120$ Oe, the contribution of H_{EB}-related energy increases to a certain extent, but the contribution of stray-field energy still dominates; hence, the Y-type-I state remains thermodynamically stable. For the nanomagnets with smaller d and L under $H_{\mathrm{EB}} = 120$ Oe, the reason why the nanomagnets can relax into Y-type-VI state is that (i) the contribution of stray-field energy decreases, the thermodynamic stability of Y-type-I state weakening; (ii) the relative contribution of Zeeman-type exchange-bias-related energy is enhanced, creating Y-type-VI state favorably with the magnetic moment parallel to the H_{EB} or at an acute angle to the H_{EB}.

Concave triangular nanomagnets, which exhibit the stable Y-type-I state lying at the boundary between Y-type-I state and Y-type-VI state and simultaneously possess a relatively high ratio of unrelaxed strain, are highly desirable for our design. Therefore, the dimension of the concave triangular nanomagnet used for the simulations is 150 nm (side length) × 5 nm (thickness), an optimized dimension that leads to the lowest critical strain and enough stability (see discussion later) for a deterministic "Y"-like magnetic state switching.

Figure 3(a) demonstrates an electric-field-manipulated "Y"-like state switching driven by a square-wave bipolar strain pulse with a duration of 6.18 ns in the triangle magnet ($L = 150$ nm, $d = 5$ nm, and $R_c = 600$ nm). The interfacial exchange-bias field H_{EB} is regarded as 120 Oe to obtain a low critical strain for the above switching (see discussions later). The initial magnetic state is Y-type-I state, as shown in Fig. 3(b). For a (011)-oriented PMN-PT film under the application of electric field, large anisotropic piezostrain ($\varepsilon_{yy} - \varepsilon_{xx}$ up to approximately 1500 ppm [30]) can be generated and transferred
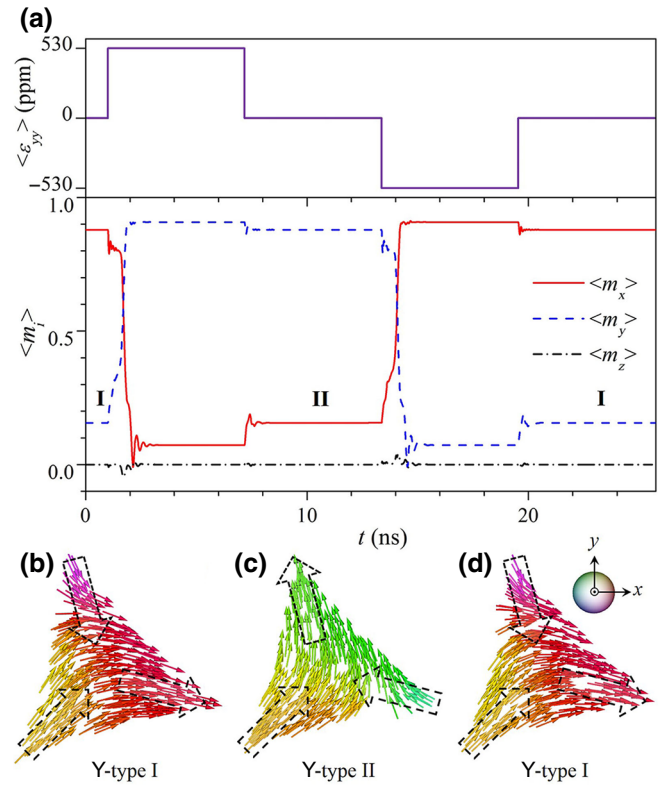

FIG. 3. (a) Electric-field-induced square-wave piezostrain (ε_{yy}) pulse with a duration of 6.18 ns (in the top panel) enabling 120° rotation of "Y"-like magnetic state and the corresponding dynamically temporal evolution of the average magnetization in the bottom panel, where $\langle m_i \rangle$ ($i = x, y, z$) represents the component of the average magnetization of the nanomagnet. (b)–(d) Snapshots of stable surface magnetization distributions corresponding to Y-type-I, Y-type-II, and back to Y-type-I states, respectively. The average magnetization in the three corners of the nanomagnet is schematically marked by the dashed-open arrows.

to Terfenol-D nanomagnet. Such an anisotropic tensile strain of 530 ppm is applied to the nanomagnet, resulting in creating a uniaxial magnetoelastic anisotropy along the y axis because of its positive magnetostrictive coefficient. Driven by co-action of strain-induced uniaxial magnetoelastic anisotropy and the exchange-bias field H_{EB}, the initial Y-type-I magnetic state is transformed into a bucklelike magnetic state [see Fig. 4(l)]. Then, after the removal of ε_{yy}, a new magnetic state with Y-type II [see Fig. 3(c)] is formed, accomplishing a 120° rotation of "Y"-like magnetic state in a deterministic manner (discussed in Fig. 4). Such a piezostrain-mediated rotation is nonvolatile because in-plane shape anisotropy offers an energy barrier separating Y-type-I and Y-type-II degenerate states. Subsequently, applying another compressive piezostrain ($\varepsilon_{yy} = -530$ ppm) along the y axis can allow similarly a Y-type-II state to be switched back to the initial Y-type-I state [Fig. 3(d)] via creating another intermediate bucklelike
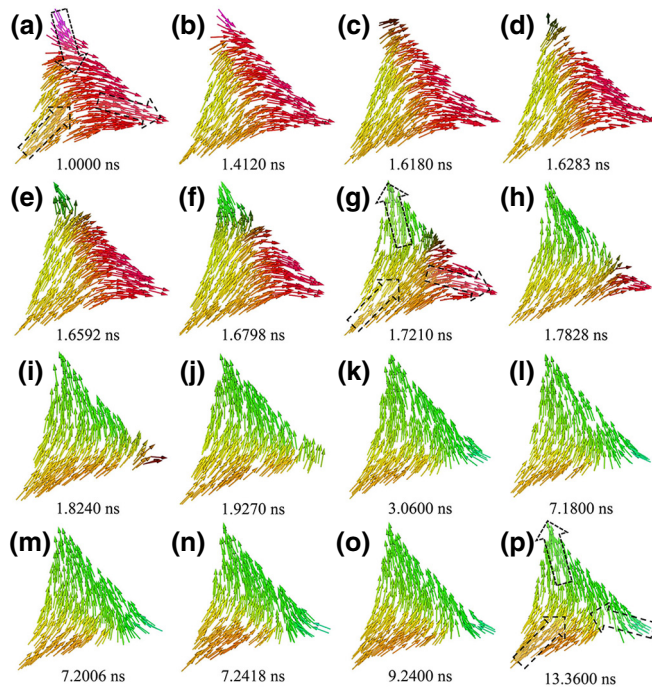
FIG. 4. Nonequilibrium dynamics of "Y"-like magnetic state switching from (a) the initial Y-type-I state to (p) Y-type-II state, and stable surface magnetization distributions at (a) 1.0000 ns, (b) 1.4120 ns, (c) 1.6180 ns, (d) 1.6283 ns, (e) 1.6592 ns, (f) 1.6798 ns, (g) 1.7210 ns, (h) 1.7828 ns, (i) 1.8240 ns, (j) 1.9270 ns, (k) 3.0600 ns, (l) 7.1800 ns, (m) 7.2006 ns, (n) 7.2418 ns, (o) 9.2400 ns, (p) 13.3600 ns, among which (l) denotes the intermediate bucklelike state.

state (see Supplemental Material [35] for details), and therefore such a rotation is also repeatable. The switching of "Y"-like magnetic state is also realized by a slower strain pulse (approximately 10.30 ns) as shown in the Supplemental Material [35], revealing that this two-step switching does not require a precise duration control of strain pulse.

Also, modeling the dynamics of magnetic switching in the patterned nanoscale heterostructures is significant to understand and control the magnetism for multiferroic device applications with fast speed. Next, we focus on nonequilibrium dynamics of "Y"-like magnetic state switching to not only fundamentally understand the mechanism of manipulating magnetic switching by electric fields but also identify the timescale limits of the dynamics governing piezostrain-mediated magnetic switching. Figures 4(a)–4(l) reveal that switching the initial Y-type-I magnetic state to the bucklelike magnetic state under the tensile piezostrain $\varepsilon_{yy} = 530$ ppm includes two dynamic processes: ① it is first switched to the transitional state of Y-type VI [see Fig. 4(g)], which is metastable state stabilized by magnetoelastic anisotropy and the H_{EB}; ② subsequently, it is switched to the intermediate bucklelike magnetic state [see Fig. 4(l)], mainly driven by

the minimization of elastic energy and exchange energy. After removing ε_{yy} in Figs. 4(m)–4(p), the bucklelike state relaxes into the Y-type-II state [see Fig. 4(p)] via the local magnetization at three corners of the nanomagnet rotating by an acute angle, rather than Y-type-I state via the local magnetization rotating by an obtuse angle through the highest local stray-field energy states [see Figs. 1(i)–1(k)]. Therefore, this 120° rotation of "Y"-like magnetic state is deterministic.

The criterion that is used to distinguish between the bucklelike state and Y-type-II state is the reduction of the total free energy. Intuitively, there exists a small difference between the bucklelike state in Fig. 4(l) and the final Y-type-II state in Fig. 4(p) from the point of view of magnetic configuration, but from the point of view of the total free-energy density f_{tot} (see Supplemental Material [35] for details), the bucklelike state at the moment when the piezostrain is removed possesses a higher energy than the final Y-type-II state as shown in the Supplemental Material [35]. The evolution for the bucklelike state relaxing into Y-type-II state is mainly driven by minimizing the elastic and intrinsic energy densities. Hence, the Y-type-II magnetic state is energetically more stable than the bucklelike state after removing the piezostrain.

Moreover, it reveals that the magnetic state at 3.06 ns (i.e., at 2.06 ns after the application of ε_{yy}) in Fig. 4(k) has approached the intermediate bucklelike state in Fig. 4(l). Similarly, the magnetic state at 9.24 ns (i.e., at 2.06 ns after the removal of ε_{yy}) in Fig. 4(o) has almost reached the stable Y-type-II state in Fig. 4(p). Also, "Y"-like state switching via a faster strain pulse (approximately 2.06 ns) is also achieved using phase-field simulations (see Supplemental Material [35] for details). Hence, the timescale limit of switching dynamics of "Y"-like magnetic state in the Terfenol-D nanomagnet can be identified as about 2 ns.

Next, we start to discuss the effect of the sizes (L, d, and R_c) of the nanomagnet and the interfacial exchange bias field H_{EB} on the critical strain (ε_{crit}) required for switching "Y"-like magnetic state to a bucklelike magnetic state in the Terfenol-D concave triangular nanomagnet. Under the fixed $d = 5$ nm and $H_{EB} = 120$ Oe, ε_{crit} increases monotonically with L increasing in Fig. 5(a), because here the smaller 5-nm-thickness nanomagnet has an overall high ratio of unrelaxed strain [see Fig. 2(a)] and the initial "Y"-like state becomes more stable at the larger L due to the enhanced shape anisotropy. Therefore, there exists a minimum critical strain about 530 ppm at $L = 150$ nm, at which the ratio of unrelaxed strain is still high and the stability of "Y"-like state is smaller than that of the larger side-length nanomagnet. Under the same $L = 150$ nm (or 250 nm) and $H_{EB} = 120$ Oe, a monotonic increase of the critical strain with d is revealed in Fig. 5(b), as a result of both the smaller ratio of unrelaxed strain and the enhanced stability of the "Y"-like state. When d and L remain at 5 nm and
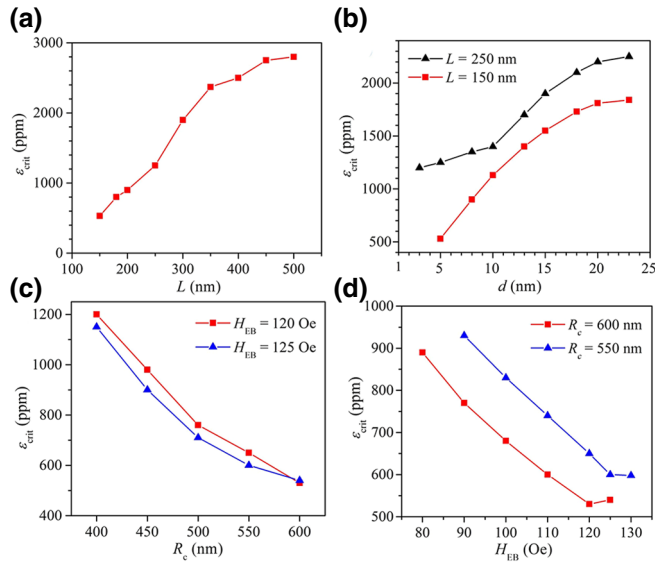
FIG. 5 (a) Influence of side length (L) on the critical strain (ε_{crit}) for switching "Y"-like state to bucklelike state in the concave triangular Terfenol-D nanomagnet with the same thickness (d) of 5 nm, concave radius (R_c) of 600 nm and exchange bias (H_{EB}) of 120 Oe. (b) Influence of d on ε_{crit} under the same $R_c = 600$ nm and $H_{EB} = 120$ Oe for different $L = 150$ nm, 250 nm. (c) Influence of R_c on ε_{crit} under a constant $d = 5$ nm and $L = 150$ nm but different $H_{EB} = 120$ Oe, 125 Oe. (d) Influence of H_{EB} on ε_{crit} under a fixed $d = 5$ nm and $L = 150$ nm but different $R_c = 550$ nm, 600 nm.

150 nm, respectively, ε_{crit} decreases with the increase of R_c under $H_{EB} = 120$ Oe in Fig. 5(c). This is because the large R_c weakens the stability of "Y"-like state.

Under the fixed $d = 5$ nm, $L = 150$ nm, and $R_c = 600$ nm (or 550 nm), ε_{crit} varies nonmonotonically but shows an overall decreasing trend as H_{EB} increases in Fig. 5(d). Such a complex feature is attributed to the different contributions of H_{EB} for two dynamical processes (as discussed in Fig. 4) during the "Y"-like-to-bucklelike magnetic state switching. When H_{EB} is small, the stability of "Y"-like state is large, which means that the large potential barrier for switching the dynamical process ① dominates, resulting in a larger ε_{crit}. Before the certain threshold of H_{EB} (i.e., 120 Oe for $R_c = 600$ nm), a larger H_{EB} can more significantly reduce the stability of the initial "Y"-like state and thereby facilitate the transformation to the bucklelike state. However, when H_{EB} (e.g., 125 Oe) is larger than the threshold of H_{EB} (=120 Oe), the potential barrier for switching the dynamical process ① is small but the barrier for switching the dynamical process ② enlarges and dominates, leading to a slightly larger ε_{crit}.

A diagram of $H_{EB} - R_c - \varepsilon_{crit}$ for robust and repeatable "Y"-like magnetic state switching under the same $L = 150$ nm and $d = 5$ nm is constructed using phase-field simulations in Fig. 6(a). When R_c is 600 nm, the initial Y-type-I state is sufficiently stable and ε_{crit} has a wide
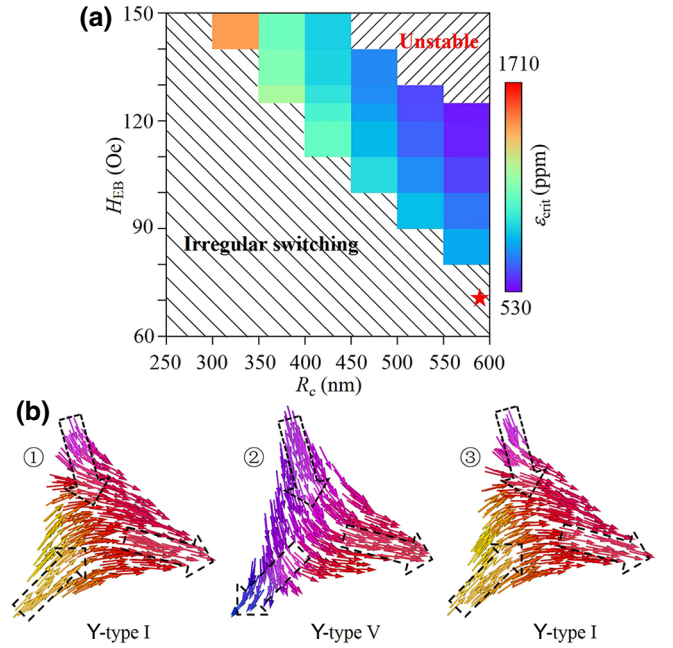

FIG. 6. (a) Diagram of H_{EB}-R_c-critical strain (ε_{crit}) for reliable magnetic state switching of Y-type mode under the same $L = 150$ nm and $d = 5$ nm. The color bar denotes the magnitude of critical strain. The region with the line pattern of "///" denotes the unstable initial state while the region with the line pattern of "\\\" means the stable initial state but an irregular switching. (b) Irregular switching (meaning that 2-in-1-out Y-type mode does not exist stably) for the initial Y-type-I state, mediated by a tensile piezostrain pulse (approximately 6.18 ns) of 890 ppm and the subsequent same magnitude of compressive piezostrain pulse in the concave triangular nanomagnet with $H_{EB} = 70$ Oe and $R_c = 600$ nm (marked by a red-colored pentagle), where stable surface magnetization states ①, ②, and ③ correspond to Y-type-I, Y-type-V, and back to Y-type-I states, respectively.

tunable range via altering H_{EB}. There exists a minimum critical strain of 530 ppm at the fixed $R_c = 600$ nm and $H_{EB} = 120$ Oe. Nevertheless, when H_{EB} and R_c fall within the top-right-corner region, the initial Y-type-I state will no longer stabilize and relax into Y-type-VI state, meaning that it cannot achieve the expected switching as given in Fig. 3. Hence, the corresponding upper limit of H_{EB} decreases with the increase of R_c as shown in Fig. 6(a). However, when H_{EB} and R_c fall within the bottom-left-corner region (i.e., the irregular switching region), the switching from Y-type-I state to Y-type-V state occurs. Compared with the switching of Y-type mode in Fig. 3, the irregular switching means that the magnetic configuration of 2-in-1-out Y-type mode does not remain unchanged but a magnetic configuration of 1-in-2-out Y-type mode (e.g., Y-type V here) is created after removing the tensile strain pulse of 890 ppm as displayed in Fig. 6(b) ②. This is mainly because the stability of the initial Y-type-I state is so large that the potential barrier for switching the dynamical process ① (see Fig. 4) cannot be overcome only by

the electric-field-induced strain unless H_{EB} or R_c increases. Subsequently, the initial state is switched to Y-type-V state. Interestingly, after applying and removing another compressive strain pulse of $\varepsilon_{yy} = -890$ ppm, the magnetic state returns to the initial Y-type-I state again, which arises from the co-action of compressive-strain-mediated uniaxial magnetoelastic anisotropy along the x axis and the H_{EB} that favors the backward switching of the Y-type-V state to Y-type-I state. It also reveals that there exists a corresponding lower limit of H_{EB} for the normal switching at the given parameter.

Figure 7(a) shows the energetics for "Y"-like magnetic state switching under the application of the tensile strain $\varepsilon_{yy} = 530$ ppm, where the optimal parameters are set as $L = 150$ nm, $d = 5$ nm, $R_c = 600$ nm, and $H_{EB} = 120$ Oe (yielding the lowest ε_{crit} of 530 ppm). Here, the intrinsic energy density ($f_{intrinsic}$) consists of stray field, exchange, and H_{EB}-related energy density. As seen, there exists an intrinsic energy-density barrier ($\Delta f_{barrier} = 1824.1$ J/m^3) for switching of an initial "Y"-like state to a bucklelike state, which is overcome by a reduction of elastic energy density

($\Delta f_{elast} = 7790.5$ J/m^3). Switching "Y"-like state to bucklelike state is driven by the minimization of exchange energy and elastic energy contribution, as displayed in Fig. 7(a), although stray-field energy and H_{EB}-related energy slightly increase.

Seen from the temporal evolution of $f_{intrinsic}$, there exist multiple transitional states (corresponding to the $f_{intrinsic}$ peaks) during the creation of the bucklelike state going through a dynamical oscillation. The time when $f_{intrinsic}$ reaches the first and the second highest peak is signified as t_{ts1} and t_{ts2} in Fig. 7(a), respectively. The local magnetization vectors at the left-corner region rotate to the orientation parallel to the side length of the triangle at $t = t_{ts1}$ in Fig. 7(c), while the Y-type-VI state starts to nucleate at $t = t_{ts2}$ as shown in Fig. 7(d). Figures 7(a) and 7(e) reveal that the total energy of the 3-ns magnetization state reaches the equilibrium value, and hence it means that the time limit of "Y"-like magnetic state switching is about 2 ns, consistent with the analysis of switching dynamics in Fig. 4.

The present work computationally demonstrates several advantages of the proposed nanoscale heterostructure over the recent report [25] in the field of electric-field-driven magnetic switching. First, compared with the mechanism of the rotation of magnetic state [25], the mechanism we propose is deterministic and an interfacial exchange-bias field from the antiferromagnet is fixed, which is more convenient for the experimental operation. Second, compared with electric-field-driven rotation of the magnetic state experimentally [25], we focus on nonequilibrium dynamics of Y-type magnetic state switching to understand the underlying physics mechanism. Third, compared with the report utilizing the magnetization switching of a Co nanodot to out-of-plane direction as the intermediate state [25], the magnetization switching process is almost within the horizontal plane because of the strong out-of-plane demagnetization. Fourth, compared with the shortest duration of 10-ns strain pulse for the switching in Ref. [25], the fastest switching speed (approximately 2 ns) is given by phase-field simulations. In general, we offer insights into the underlying physics of switching this exotic Y-type magnetic state and demonstrate that the proposed nanoscale multiferroic heterostructure offers a viable path to implementing such a spin memory device with fast speed and low power.
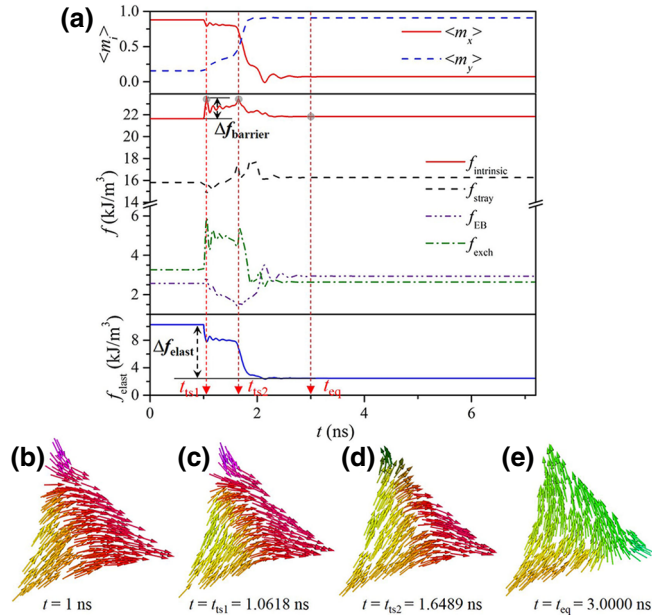
FIG. 7. (a) Dynamic temporal evolution of the average intrinsic energy density (including stray field, exchange, and H_{EB}-related energy density) (middle panel) and elastic energy density (bottom panel) during the switching from an initial Y-type-I state to a bucklelike state upon applying a tensile piezostrain $\varepsilon_{yy} = 530$ ppm, where the corresponding temporal evolutions of the average magnetization lie at the top panel. The angle bracket denotes the volumetric average. The gray dots along with the downward arrows signify the transitional states of the highest $f_{intrinsic}$ at $t = t_{ts1}$, the second highest $f_{intrinsic}$ at $t = t_{ts2}$ and the equilibrium state at $t = t_{eq}$. (b)–(e) The corresponding magnetization distributions at the initial state, the transitional states of t_{ts1} and t_{ts2}, and equilibrium state t_{eq}, respectively.

IV. CONCLUSION

To summarize, we computationally demonstrate a deterministic, nonvolatile, robust, and repeatable 120° rotation of "Y"-like magnetic state purely driven by electric-field-induced strain in a patterned nanoscale multiferroic heterostructure consisting of an amorphous Terfenol-D concave triangular nanomagnet on top of Pb(Mg$_{1/3}$Nb$_{2/3}$)O$_3$-PbTiO$_3$ film. We find that the "Y"-like magnetic state

switching is involved with two dynamic processes: (i) converting a Y-type I state into a bucklelike state by the congenerous effect of strain-mediated uniaxial magnetoelastic anisotropy and the H_{EB}; (ii) relaxing into Y-type II state driven by minimizing stray-field energy after removing strain. It is also shown that "Y"-like state switching can be realized using a pulsed strain pulse (e.g., its duration varying from a few nanoseconds to ten nanoseconds longer) because the two-step switching obviates a precise timing control of strain pulse. Furthermore, nonequilibrium dynamics of magnetic state switching reveals that the timescale limit of switching speed is as fast as about 2 ns, and "Y"-like state switching goes through a transitional state of Y-type-VI state. Our results indicate that the critical strain reaches the lowest (530 ppm) at the moderately large H_{EB}, a shorter side length, a smaller thickness and a relatively large concave radius of the nanomagnet (Fig. 6). We also show that an upper and a lower limit of H_{EB} exist, ensuring that the stability of the initial state is neither too large nor too small in order to achieve the normal switching. Therefore, these findings are expected to motivate not only experimental and engineering efforts into fundamental understanding of electrically driven deterministic magnetic switching but also provide a technologically feasible route to designing energy-efficient, very fast, nonvolatile, and high-density spintronic memories or logic based on the proposed patterned nanoscale multiferroic heterostructures.

[1] J. Scott, Data storage: Multiferroic memories, Nat. Mater. **6,** 256 (2007).

[2] J.-M. Hu and C.-W. Nan, Opportunities and challenges for magnetoelectric devices, APL Mater. **7,** 080905 (2019).

[3] M. Trassin, Low energy consumption spintronics using multiferroic heterostructures, J. Phys.: Condens. Matter **28,** 033001 (2016).

[4] B. Peng, Z. Zhou, T. Nan, G. Dong, M. Feng, Q. Yang, X. Wang, S. Zhao, D. Xian, Z.-D. Jiang, W. Ren, Z.-G. Ye, N. X. Sun, and M. Liu, Deterministic switching of perpendicular magnetic anisotropy by voltage control of spin reorientation transition in $(Co/Pt)_3/Pb(Mg1/3Nb_{2/3})O_3–PbTiO_3$ multiferroic heterostructures, ACS Nano **11,** 4337 (2017).

[5] N. A. Spaldin and R. Ramesh, Advances in magnetoelectric multiferroics, Nat. Mater. **18,** 203 (2019).

[6] T. Taniyama, Electric-field control of magnetism via strain transfer across ferromagnetic/ ferroelectric interfaces, J. Phys. Condens. Matter **27,** 504001 (2015).

[7] M. Liu, O. Obi, J. Lou, Y. Chen, Z. Cai, S. Stoute, M. Espanol, M. Lew, X. Situ, and K. S. Ziemer, Giant electric field tuning of magnetic properties in multiferroic ferrite/ferroelectric heterostructures, Adv. Funct. Mater. **19,** 1826 (2009).

[8] Y. Wang, J. Li, and D. Viehland, Magnetoelectrics for magnetic sensor applications: Status, challenges and perspectives, Mater. Today **17,** 269 (2014).

[9] M. Ghidini, R. Pellicelli, J. Prieto, X. Moya, J. Soussi, J. Briscoe, S. Dunn, and N. Mathur, Non-volatile electrically-driven repeatable magnetization reversal with no applied magnetic field, Nat. Commun. **4,** 1453 (2013).

[10] M. Buzzi, R. Chopdekar, J. Hockel, A. Bur, T. Wu, N. Pilet, P. Warnicke, G. Carman, L. Heyderman, and F. Nolting, Single Domain Spin Manipulation by Electric Fields in Strain Coupled Artificial Multiferroic Nanostructures, Phys. Rev. Lett. **111,** 027204 (2013).

[11] M. Liu, T. Nan, J.-M. Hu, S.-S. Zhao, Z. Zhou, C.-Y. Wang, Z.-D. Jiang, W. Ren, Z.-G. Ye, L.-Q. Chen, and N. X. Sun, Electrically controlled non-volatile switching of magnetism in multiferroic heterostructures via engineered ferroelastic domain states, NPG Asia Mater. **8,** e316 (2016).

[12] R.-C. Peng, J.-M. Hu, L.-Q. Chen, and C.-W. Nan, On the speed of piezostrain-mediated voltage-driven perpendicular magnetization reversal: A computational elastodynamics-micromagnetic phase-field study, NPG Asia Mater. **9,** e404 (2017).

[13] M. Ghidini, B. Zhu, R. Mansell, R. Pellicelli, A. Lesaine, X. Moya, S. Crossley, B. Nair, F. Maccherozzi, C. H. W. Barnes, R. P. Cowburn, S. S. Dhesi, and N. D. Mathur, Voltage control of magnetic single domains in Ni discs on ferroelectric $BaTiO_3$, J. Phys. D: Appl. Phys. **51,** 224007 (2018).

[14] T. H. E. Lahtinen, K. J. A. Franke, and S. V. Dijken, Electric-field control of magnetic domain wall motion and local magnetization reversal, Sci. Rep. **2,** 258 (2012).

[15] J. T. Heron, J. L. Bosse, Q. He, Y. Gao, M. Trassin, L. Ye, J. D. Clarkson, C. Wang, J. Liu, S. Salahuddin, D. C. Ralph, D. G. Schlom, J. Iniguez, B. D. Huey, and R. Ramesh, Deterministic switching of ferromagnetism at room temperature using an electric field, Nature **516,** 370 (2014).

[16] Q. Yang, L. Wang, Z. Zhou, S. Zhao, G. Dong, Y. Chen, T. Min, and M. Liu, Ionic liquid gating control of RKKY

interaction in FeCoB/Ru/FeCoB and $(Pt/Co)_2/Ru/(Co/Pt)_2$ multilayers, Nat. Commun. **9**, 991 (2018).

[17] C.-G. Duan, S. Jaswal, and E. Tsymbal, Predicted Magnetoelectric Effect in Fe/BaTiO₃ Multilayers: Ferroelectric Control of Magnetism, Phys. Rev. Lett. **97**, 047201 (2006).

[18] F. Matsukura, Y. Tokura, and H. Ohno, Control of magnetism by electric fields, Nat. Nanotechnol. **10**, 209 (2015).

[19] D. K. Koltsov, R. P. Cowburn, and M. E. Welland, Micromagnetics of ferromagnetic equilateral triangular prisms, J. Appl. Phys. **88**, 5315 (2000).

[20] B. Lambson, Z. Gu, M. Monroe, S. Dhuey, A. Scholl, and J. Bokor, Concave nanomagnets: Investigation of anisotropy properties and applications to nanomagnetic logic, Appl. Phys. A **111**, 413 (2013).

[21] R.-C. Peng, J.-M. Hu, T. Yang, X. Cheng, J.-J. Wang, H.-B. Huang, L.-Q. Chen, and C.-W. Nan, Switching the chirality of a magnetic vortex deterministically with an electric field, Mater. Res. Lett. **6**, 669 (2018).

[22] S. Yakata, M. Miyata, S. Nonoguchi, H. Wada, and T. Kimura, Control of vortex chirality in regular polygonal nanomagnets using in-plane magnetic field, Appl. Phys. Lett. **97**, 222503 (2010).

[23] M. Jaafar, R. Yanes, D. P. D. Lara, O. Chubykalo-Fesenko, A. Asenjo, E. M. Gonzalez, J. V. Anguita, M. Vazquez, and J. L. Vicent, Control of the chirality and polarity of magnetic vortices in triangular nanodots, Phys. Rev. B **81**, 054439 (2010).

[24] K. Nanayakkara, I. S. Vasilevskii, I. S. Eremin, O. S. Kolentsova, N. I. Kargin, A. Anferov, and A. Kozhanov, Tunable configurational anisotropy of concave triangular nanomagnets, J. Appl. Phys. **119**, 233906 (2016).

[25] J. Yao, X. Song, X. Gao, G. Tian, P. Li, H. Fan, Z. Huang, W. Yang, D. Chen, Z. Fan, M. Zeng, and J.-M. Liu, Electrically driven reversible magnetic rotation in nanoscale multiferroic heterostructures, ACS Nano **12**, 6767 (2018).

[26] T. Zhao, A. Scholl, F. Zavaliche, K. Lee, M. Barry, A. Doran, M. P. Cruz, Y. H. Chu, C. Ederer, N. A. Spaldin, R. R. Das, D. M. Kim, S. H. Baek, C. B. Eom, and R. Ramesh, Electrical control of antiferromagnetic domains in multiferroic BiFeO₃ films at room temperature, Nat. Mater. **5**, 823 (2006).

[27] J.-M. Hu, T. Yang, J. Wang, H. Huang, J. Zhang, L.-Q. Chen, and C.-W. Nan, Purely electric-field-driven perpendicular magnetization reversal, Nano Lett. **15**, 616 (2015).

[28] R.-C. Peng, J.-M. Hu, K. Momeni, J.-J. Wang, L.-Q. Chen, and C.-W. Nan, Fast 180° magnetization switching in a strain-mediated multiferroic heterostructure driven by a voltage, Sci. Rep. **6**, 27561 (2016).

[29] M. Yi, B.-X. Xu, and Z. Shen, 180o magnetization switching in nanocylinders by a mechanical strain, Extreme Mech. Lett. **3**, 66 (2015).

[30] T. Wu, A. Bur, P. Zhao, K. P. Mohanchandra, K. Wong, K. L. Wang, C. S. Lynch, and G. P. Carman, Giant electric-field-induced reversible and permanent magnetization reorientation on magnetoelectric Ni/(011)[Pb($Mg_{1/3}Nb_{2/3}$)O₃]$_{(1-x)}$-[PbTiO₃]$_x$ heterostructure, Appl. Phys. Lett. **98**, 012504 (2011).

[31] M. Liu, S. Li, Z. Zhou, S. Beguhn, J. Lou, F. Xu, T.-J. Lu, and N. X. Sun, Electrically induced enormous magnetic anisotropy in terfenol-D/lead zinc niobate-lead titanate multiferroic heterostructures, J. Appl. Phys. **112**, 063917 (2012).

[32] J.-X. Zhang and L.-Q. Chen, Phase-field microelasticity theory and micromagnetic simulations of domain structures in giant magnetostrictive materials, Acta Mater. **53**, 2845 (2005).

[33] M. E. Schabes and A. Aharoni, Magnetostatic interaction fields for a 3-dimensional array of ferromagnetic cubes, IEEE Trans. Magn. **23**, 3882 (1987).

[34] A. G. Khachaturyan, *Theory of Structural Transformations in Solids* (Dover Publications, 2008).

[35] See Supplemental Material at http://link.aps.org/supplemental/10.1103/PhysRevApplied.13.064018 for elastic stiffness tensor of the isotropic Terfenol-D, effect of the ferroelectric layer thickness on strain relaxation of the nanomagnet, spatial distribution of the magnetization and strain distribution in the nanomagnet, "Y"-like domain switching driven by a slower strain pulse and a faster strain pulse, energy analysis for the bucklelike state relaxing into Y-type-II state, and effect of lateral dimensions of the system grid on strain relaxation of the nanomagnet.

[36] Y.-L. Li, S.-Y. Hu, Z.-K. Liu, and L.-Q. Chen, Effect of substrate constraint on the stability and evolution of ferroelectric domain structures in thin films, Acta Mater. **50**, 395 (2002).

[37] G. S. Abo, Y.-K. Hong, J. Park, J. Lee, W. Lee, and B.-C. Choi, Definition of magnetic exchange length, IEEE Trans. Magn. **49**, 4937 (2013).

[38] G. Dewar, Effect of the large magnetostriction of terfenol-D on microwave transmission, J. Appl. Phys. **81**, 5713 (1997).

[39] D. B. Gopman, J. W. Lau, K. P. Mohanchandra, K. Wetzlar, and G. P. Carman, Determination of the exchange constant of $Tb_{0.3}Dy_{0.7}Fe_2$ by broadband ferromagnetic resonance spectroscopy, Phys. Rev. B **93**, 064425 (2016).

[40] J.-J. Wang, T.-N. Yang, J. A. Zorn, E. Wang, J. Irwin, S. Lindemann, M. S. Rzchowski, J.-M. Hu, C.-B. Eom, and L.-Q. Chen, Strain anisotropy and magnetic domain structures in multiferroic heterostructures: High-throughput finite-element and phase-field studies, Acta Mater. **176**, 73 (2019).